Dispersive charge transfer state electroluminescence in organic solar cells

Raju Lampande,[#] Adrian Pizano,[#] Manting Gui, Robert C. Cawthorn, Barry P. Rand, and Noel C. Giebink[*]

R. Lampanda, A. Pizano, R. C. Cawthorn, N. C. Giebink

Department of Electrical Engineering, The Pennsylvania State University, University Park, Pennsylvania 16802, USA

N. C. Giebink

Department of Electrical Engineering and Computer Science, University of Michigan, Ann Arbor, Michigan 48109, USA

M. Gui, B. P. Rand

Department of Electrical Engineering, Princeton University, Princeton, New Jersey 08544, USA

B. P. Rand

Andlinger Center for Energy and the Environment, Department of Electrical Engineering, Princeton University, Princeton, New Jersey 08544, USA

This is the author manuscript accepted for publication and has undergone full peer review but has not been through the copyediting, typesetting, pagination and proofreading process, which may lead to differences between this version and the Version of Record. Please cite this article as doi: 10.1002/aenm.202300394.

[#]These authors contributed equally to this work

E-mail: ngiebink@umich.edu

Keywords: organic photovoltaic, non-equilibrium, disorder, relaxation, density of states

The notion of quasi-equilibrium is central to most solar cells; however, it has been questioned in organic photovoltaics (OPVs) owing to strong energetic disorder that frustrates efficient relaxation of electrons and holes within their respective density of states (DOS). Here, we apply modulation electroluminescence (EL) spectroscopy to OPVs and find that the frequency response of charge transfer (CT) state EL on the high energy side of the spectrum differs from that of the low energy side. This observation confirms that static disorder contributes substantially to the linewidth of the steady-state EL spectrum and is unambiguous proof that the distribution of CT states formed by electrical injection in the dark is not in quasi-equilibrium. These results emphasize the need for caution when analyzing OPV cells on the basis of reciprocity models that assume quasi-equilibrium holds, and highlight a new method to study this unusual aspect of OPV operation.

1. Introduction

Charge separation and recombination govern the efficiency of every solar cell. In most cases, these processes are well-described by assuming quasi-equilibrium, which implies that the relaxation of electrons and holes within their respective density of states (DOS) is fast compared to all other

charge transport and recombination timescales[1,2]. This allows Boltzmann-like electron and hole distributions to be established and greatly simplifies device modeling[1,2].

Recent observations that suggest photogenerated charges are extracted from organic photovoltaic (OPV) cells before they attain a thermal distribution within the DOS[3–7] have therefore led to debate over the extent to which quasi-equilibrium concepts are appropriate for OPVs[8–13]. On the one hand, non-equilibrium effects such as dispersive transport (where the mobility of photogenerated charge carriers decreases with time) and spectral diffusion (where the photoluminescence exhibits a dynamic red-shift) are well-established for disordered organic semiconductors and are consistent with slow relaxation in the DOS predicted by kinetic Monte Carlo (kMC) modeling[7,14–16]. On the other hand, there is a vast amount of data demonstrating that quasi-equilibrium drift-diffusion modeling and reciprocity analyses adequately describe OPV cell operation[17–21].

At the center of this debate is the energetically-disordered distribution of charge transfer (CT) states that influence charge separation, recombination, and energy loss of OPVs [22–24]. To a first approximation, the CT DOS is a convolution of the electron and hole DOS at the donor-acceptor (DA) interface, less the CT state binding energy[25,26]. While non-equilibrium occupation of the CT DOS seems plausible under illumination where efficient D→A charge transfer populates the DOS uniformly (i.e. far from equilibrium), quasi-equilibrium would nominally be expected to hold in the dark since thermal electrons and holes are injected from the contacts. Indeed, this assumption underlies the photovoltaic reciprocity relations that are widely used to analyze OPVs[18,20,21].

Here, we apply modulation electroluminescence spectroscopy (MELS)[27–29] to demonstrate that CT EL from both bulk and planar heterojunction small molecule OPV cells is dispersive. That is,

CT emission on the high energy side of the electroluminescence (EL) spectrum exhibits a different modulation response (i.e. magnitude and phase as a function of modulation frequency, in direct analogy to impedance spectroscopy) than CT emission on the low energy side of the EL spectrum. Since dispersive EL is not possible for a quasi-equilibrium distribution of CT states, this observation directly confirms kMC modeling by Melianas et *al.*[5] that argues for non-equilibrium occupation of the CT DOS in the dark. It also confirms that static disorder contributes non-negligibly to the linewidth and behavior of the CT EL spectrum[30]. These results highlight a new approach to identify and study non-equilibrium occupation in the CT DOS, and solidify the need for modeling methods that can account for this unusual aspect of OPV operation.

2. Results and Discussion

2.1. Modulation response of CT emission

We study the small molecule DA system shown in the inset of **Figure 1a**, which consists of the donor 4,4',4''-tris[(3-methylphenyl)phenylamino]triphenylamine (MTDATA) and acceptor 4,7-diphenyl-1,10-phenanthroline (BPhen). Blends of MTDATA:BPhen emit photoluminescence (PL) and EL that is red-shifted and broadened relative to the Frenkel exciton emission of each individual material (Figure 1b)[31,32]. Although sometimes referred to as an exciplex in the organic light-emitting diode (OLED) literature, the interfacial excitation in MTDATA:BPhen and other systems like it[16,33,34] is, in fact, a CT state, as evident from efficient photocurrent generation (Figure 1d), a high open-circuit voltage (Figure 1c), and ground state CT absorption (which does not exist for an exciplex) in the photocurrent external quantum efficiency (EQE) spectrum (Figure 1d). When operated as OLEDs

under forward bias in the dark, these devices emit efficient CT EL (peak EQE >5%) with a turn-on voltage of approximately 2 V (Figure 1a), similar to those studied in Ref. [31].

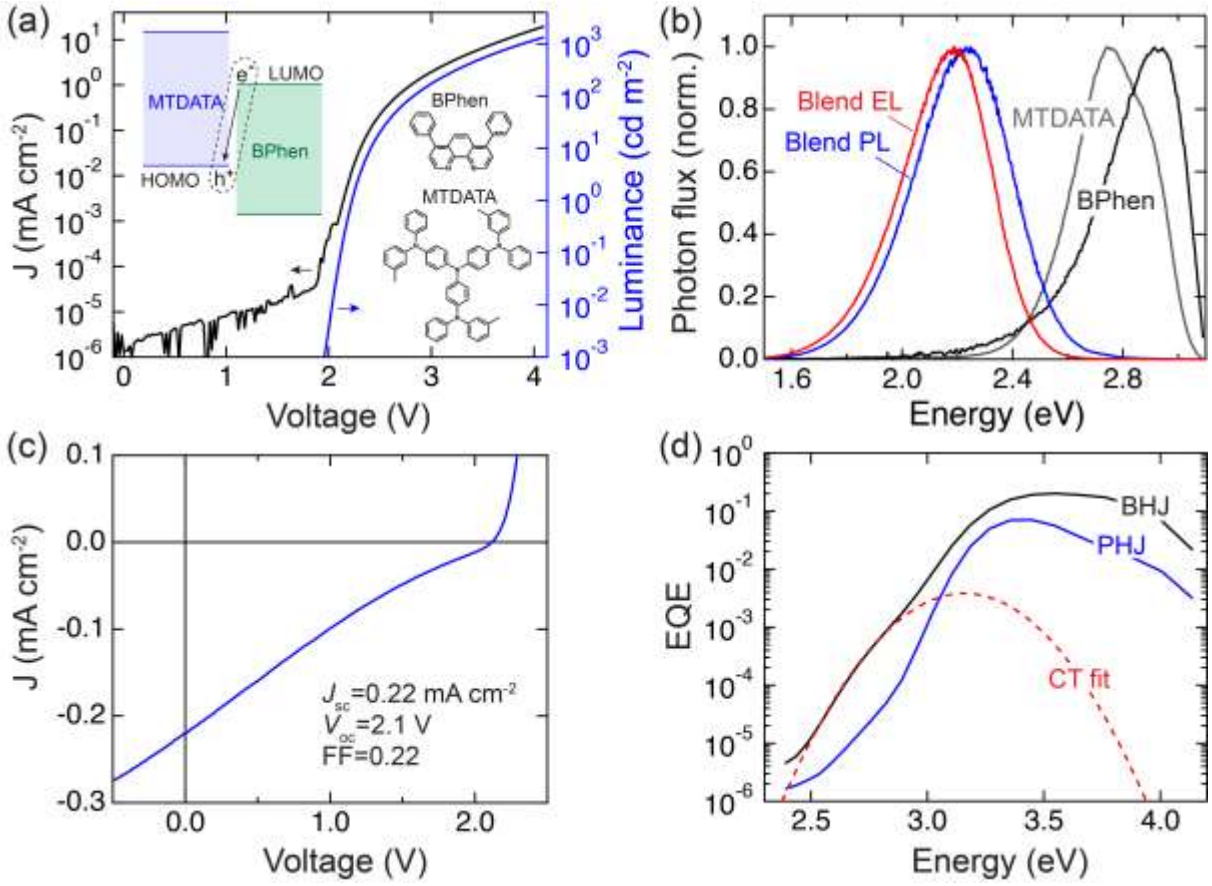

Figure 1. (a) Current density-voltage-luminance (*J-V-L*) characteristic for a bulk heterojunction (BHJ) device with an organic layer stack consisting of MTDATA (10 nm)/1:1 MTDATA:BPhen (60 nm)/Bphen (10 nm). The inset diagram illustrates the process of CT state recombination at the DA interface that leads to light emission. **(b)** PL spectra of neat MTDATA and BPhen films compared to that of a 1:1 MTDATA:BPhen blend film. The EL spectrum of the device from panel (a) is also shown for comparison. **(c)** *J-V* characteristic for a similar MTDATA (10 nm)/1:1 MTDATA:BPhen (40 nm)/Bphen (10 nm) BHJ device operated in photovoltaic mode under simulated 1 sun illumination. **(d)** Photocurrent EQE spectrum for the device in (c) measured at short circuit. The dashed red line

highlights the ground state CT absorption fit by a Marcus Gaussian lineshape using effective reorganization and CT state energies of 0.71 eV and 2.45 eV, respectively. The EQE spectrum of an MTDATA (50 nm)/BPhen (50 nm) planar heterojunction (PHJ) device shown in blue exhibits weaker CT state absorption that is consistent with the reduction in DA interface area.

The efficient CT emission from these devices enables their recombination dynamics to be studied via MELS using the experimental setup shown in the top portion of **Figure 2a**. Briefly, the device is excited using the force terminals of an impedance analyzer while EL is detected using a photomultiplier tube, converted to a voltage via a high-speed transimpedance amplifier, and then read out between the sense terminals of the impedance analyzer. The signal output from the impedance analyzer is therefore the ratio of the complex EL intensity (magnitude and phase) to the complex current density or, in other words, a frequency-dependent complex quantum efficiency. This technique has previously been used to study defect and tail states in inorganic LEDs[27–29], but has yet to be applied to organic solar cells.

Figure 2b shows a Cole-Cole plot of the impedance spectra recorded for a typical device at DC current densities ranging from 10 µA cm^{-2} to 4 mA cm^{-2}. Figure 2c and 2d present Bode plots of the corresponding MELS magnitude and phase angle, respectively. The basic trends are physically intuitive insofar as increasing the DC bias leads to higher electron and hole densities, which makes recombination faster, thereby decreasing the recombination resistance of the device (causing the Cole-Cole semicircle to shrink) and pushing the MELS corner frequency higher. The data can be quantitatively understood using the simplified kinetic scheme in Figure 2a, which motivates the

following set of rate equations to describe the time-dependent electron, hole, and CT state density (n, p, and s, respectively) in the recombination zone of width a:

$$\frac{dn}{dt} = \frac{dp}{dt} = \frac{J_\mathrm{r}}{qa} - \gamma np \,, \tag{1a}$$

$$\frac{ds}{dt} = \gamma np - \frac{s}{\tau_\mathrm{ct}}. \tag{1b}$$

Equation (1) assumes perfect charge balance, with all of the injected electron and hole current (J_r; the electronic charge is q) recombining bimolecularly (with Langevin rate coefficient, γ) to form CT states that subsequently decay with time constant, τ_ct, to the ground state. Other processes that likely also occur, such as CT state re-dissociation and intersystem/reverse intersystem crossing between singlet and triplet CT states[32], can be included (see the Supplementary Material for details), but are not required to fit the data and are therefore neglected in favor of a minimalistic model.

Assuming $n = p$ together with a harmonic time dependence for each variable (i.e. $n(t) = n_0 + \tilde{n}e^{i\omega t}$ and $J_\mathrm{r}(t) = J_\mathrm{r0} + \tilde{J}_\mathrm{r}e^{i\omega t}$), it is straightforward to obtain $\tilde{n} = \tilde{J}_\mathrm{r}/qa(i\omega + 2\gamma n_0)$ and $\tilde{s} = 2\gamma n_0 \tilde{n}/(i\omega + \tau_\mathrm{ct}^{-1})$, where the DC electron density (n_0) is set by the DC recombination current density (J_r0) according to $n_0 = (J_\mathrm{r0}/qa\gamma)^{1/2}$. Including the series resistance (R_s) and geometric capacitance (C_g) of the device from the equivalent circuit model in Figure 2a yields its impedance:

$$\tilde{Z} = R_\mathrm{s} + \frac{R_\mathrm{rec}}{1 + i\omega R_\mathrm{rec}\left(C_\mu + C_\mathrm{g}\right)}, \tag{2}$$

in terms of the chemical capacitance, C_μ, and recombination resistance, R_{rec}. Given that the AC output photon flux ($\tilde{L}$) is directly proportional to the CT state density via $\tilde{L} = a\phi_{\mathrm{oc}}\phi_{\mathrm{pl}}\tau_{\mathrm{ct}}^{-1}\tilde{s}$ (where ϕ_{oc} and ϕ_{pl} are the optical outcoupling efficiency of the device and the CT photoluminescence quantum yield, respectively), and the recombination current is related to the total current via $\tilde{J}_{\mathrm{r}}/\tilde{J} = \left[1 + i\omega R_{\mathrm{rec}}C_\mu\right]\left[1 + i\omega R_{\mathrm{rec}}\left(C_\mu + C_{\mathrm{g}}\right)\right]^{-1}$, the MELS response is therefore:

$$\tilde{M} = q\tilde{L}/\tilde{J} = \frac{\phi_{\mathrm{oc}}\phi_{\mathrm{pl}}}{(1 + i\omega\tau_{\mathrm{rec}})(1 + i\omega\tau_{\mathrm{ct}})}\left[\frac{1 + i\omega R_{\mathrm{rec}}C_\mu}{1 + i\omega R_{\mathrm{rec}}\left(C_\mu + C_{\mathrm{g}}\right)}\right]. \quad (3)$$

In Equation (3), $\tau_{\mathrm{rec}} = (2\gamma n_0)^{-1} = R_{\mathrm{rec}}C_\mu$ is the recombination lifetime of electrons and holes in the device at a given DC carrier density, n_0, which scales with the square root of the DC current density as noted above. Since $C_{\mathrm{g}} \ll C_\mu$ for the operating conditions of a typical MELS experiment, the right-hand term in brackets is approximately unity and the normalized MELS transfer function (relative to $\omega = 0$) reduces to:

$$\tilde{H}_{\mathrm{MELS}}(\omega) = \tilde{M}/M_0 = \frac{1}{(1 + i\omega\tau_{\mathrm{ct}})(1 + i\omega\tau_{\mathrm{rec}})}. \quad (4)$$

The red fit lines in Figure 2b-2d demonstrate that this simple model can describe all of the impedance and MELS data in terms of two time constants, τ_{rec} and τ_{ct}, which correspond to electron-hole recombination (formation of CT states) and natural CT state decay, respectively. At low bias (i.e. $J_0 = 10$ μA cm^{-2}), when the carrier density in the device is small and the recombination rate is correspondingly slow, the poles associated with τ_{rec} and τ_{ct} in Equation (4) are both visible in the MELS phase response (Figure 2d). As the carrier density increases with bias and recombination becomes faster (τ_{rec} decreases from 226 μs to 2.6 μs as J_0 increases from 10 μA cm^{-2} to 4 mA cm^{-2}), the recombination pole moves to higher frequency, burying the CT lifetime pole in the phase

response. The lifetime associated with the latter (τ_{ct}~10 µs) is consistent with the transient CT photoluminescence decay provided in the Supplementary Material.

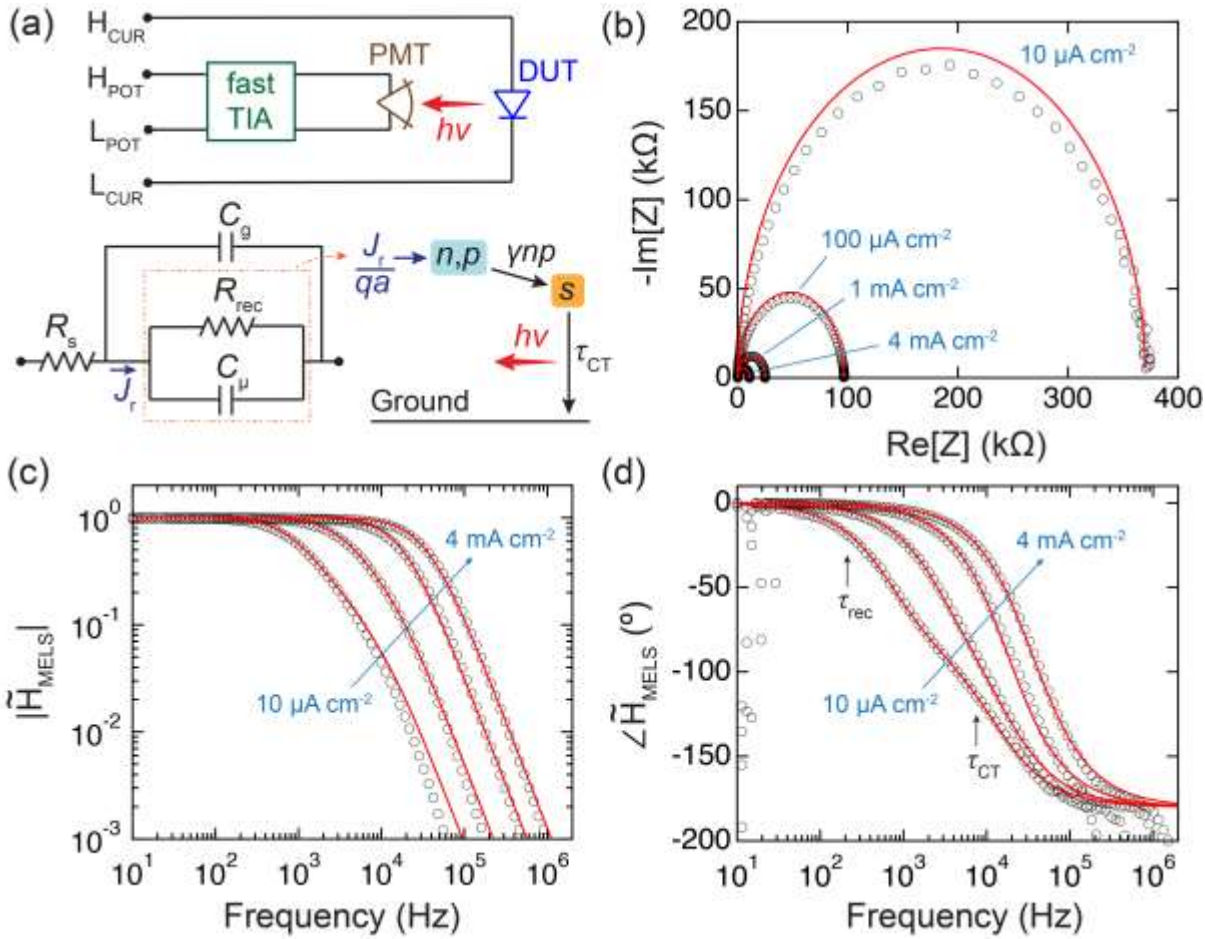

Figure 2. (a) Experimental setup of the MELS measurement (top) along with the equivalent circuit model of the device and a diagram of the recombination kinetics taking place in its emissive layer (corresponding to the orange boxed region of the equivalent circuit). TIA: transimpedance amplifier; PMT: photomultiplier tube; DUT: device under test. **(b)** Cole-Cole plot of the electrical impedance measured for the device from Figure 1a at different biases that produce the indicated DC current densities. Open circles are the measured data points and solid red lines are fits to the model in the text. **(c)** Magnitude of the MELS response at each bias, normalized to its value at low frequency. **(d)**

Corresponding phase angle of the MELS response; the sharp fall-off in phase angle below -180º that occurs at high frequency is an artifact of very low signal per the magnitude response in panel (c). Note, the MELS and impedance data are collected sequentially because the cable connections must be changed to go from one measurement to the other. All of the parameters used to fit the data in (b)-(d) are summarized in the Supplementary Material.

2.2. Dispersive CT emission

Figure 3a,b shows the MELS response of the same device, but with the emitted light collected through a series of bandpass filters spanning the CT EL spectrum (Figure 3a, inset). Crucially, the data show that the CT EL is dispersive, meaning that emission from the high energy side of the spectrum responds *faster* to the AC current modulation than emission from the low energy side of the spectrum, as evident from the reduced magnitude roll-off and phase delay of the former at high frequency. The same behavior is observed for planar heterojunction MTDATA:BPhen devices (see the Supplementary Material), but not for a tris(8-hydroxyquinolinato)aluminum (Alq_3)/N,N'-bis(naphthalen-1-yl)-N,N'-bis(phenyl)benzidine (NPB) OLED with a similar emission spectrum, where EL originates from intramolecular Frenkel excitons (Figure 3c,d) instead of intermolecular CT states.

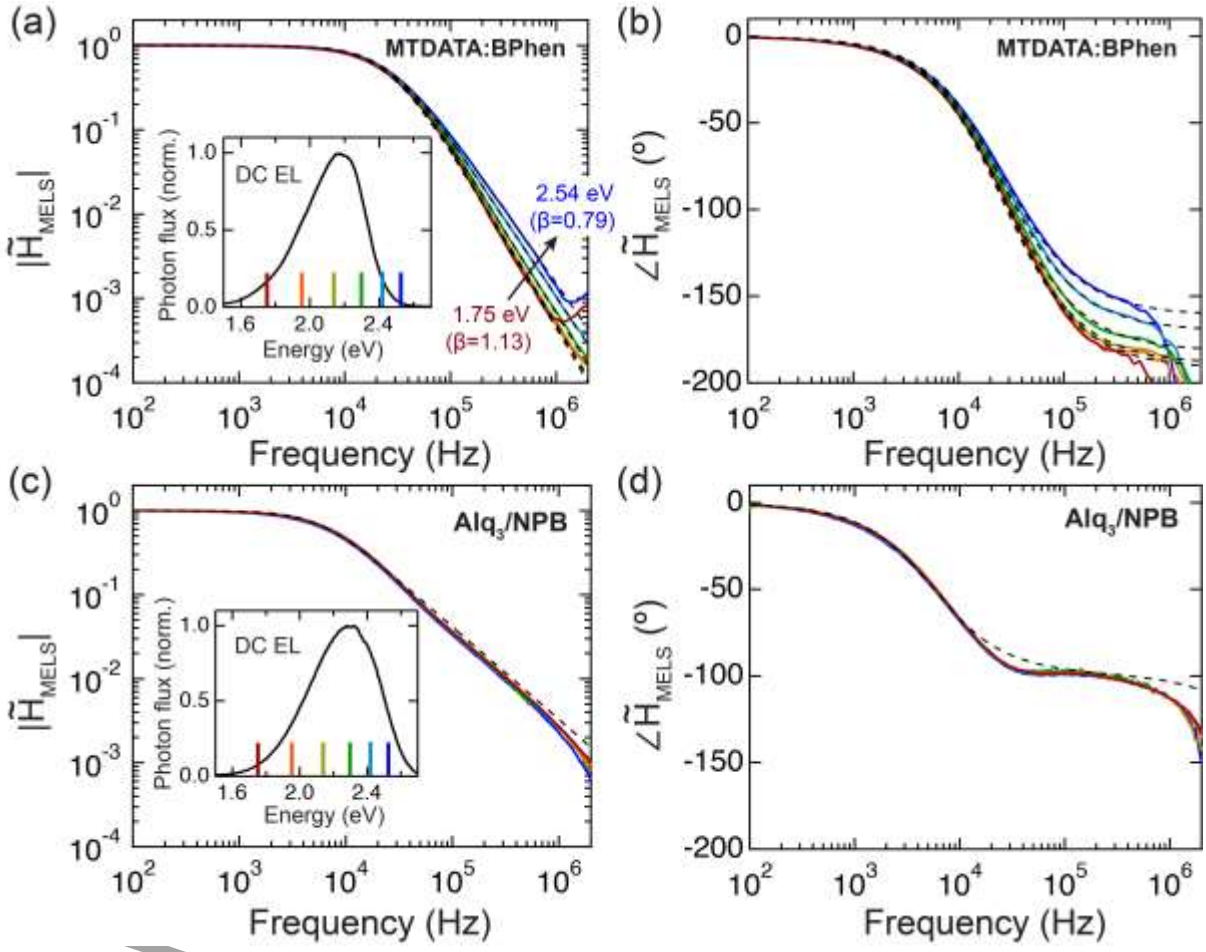

Figure 3. (a) Magnitude of the MELS response measured for the MTDATA:BPhen device from Figure 2 at different photon energies across the CT EL spectrum shown in the inset. The bias corresponds to a DC current density of 2 mA cm^{-2}. **(b)** Corresponding MELS phase response. Black dashed lines indicate fits to the Cole-Davidson form of $\widetilde{H}_{\mathrm{MELS}}$ described in the text by varying β as indicated, with τ_{ct} and τ_{rec} fixed at 4 µs and 58 µs, respectively. **(c, d)** Similar MELS magnitude and phase data collected for a bilayer Alq$_3$/NPB OLED. No dispersion is observed as a function of emission energy in this case. Setting τ_{ct} to 13 ns (i.e. the exciton lifetime of Alq$_3$) with $\beta = 1.1$ captures the single pole MELS magnitude and phase response at frequencies well below τ_{ct}^{-1}.

We find that the MELS dispersion of the MTDATA:BPhen devices can be described by adding a Cole-Davidson parameter[35], β, to the recombination term in Equation (4), namely $\widetilde{H}_{\mathrm{MELS}}(\omega) = (1 + i\omega\tau_{\mathrm{ct}})^{-1}(1 + i\omega\tau_{\mathrm{rec}})^{-\beta}$. Physically, the Cole-Davidson parameter in this expression reflects a distribution of different recombination time constants, τ, with $\beta < 1$ ($\beta > 1$) indicating that the distribution is weighted more (less) heavily toward time constants below the nominal value of τ_{rec}; see the Supplementary Material for more details[35,36]. As shown in Figure 3a,b, the emission energy dependence of the MELS spectra can be reproduced simply by varying β with fixed values of τ_{ct} and τ_{rec}.

While the exact form of the distribution function associated with the Cole-Davidson frequency response is not particularly meaningful, its statistical moments are [37]. Specifically, the average logarithmic recombination time constant, $\langle \ln \tau \rangle$, is a robust descriptor of the data and can be calculated from β according to $\langle \ln \tau \rangle = \ln \tau_{\mathrm{rec}} + \psi(\beta) + 0.58$, where ψ is the digamma function [37]. Thus, the energy-dependent variation in β used to fit the data in Figure 3a,b uniquely determines the *change* in average logarithmic recombination time across the CT spectrum (**Figure 4**), quantifying the qualitative observation above that higher energy CT emission responds 'faster' to the current modulation. Figure 4 also shows that, while there is relatively little change in the lineshape of the DC EL spectrum with decreasing temperature (Figure 4a), there is a substantial increase in its frequency dispersion moving from low to high CT state energy (Figure 4b).

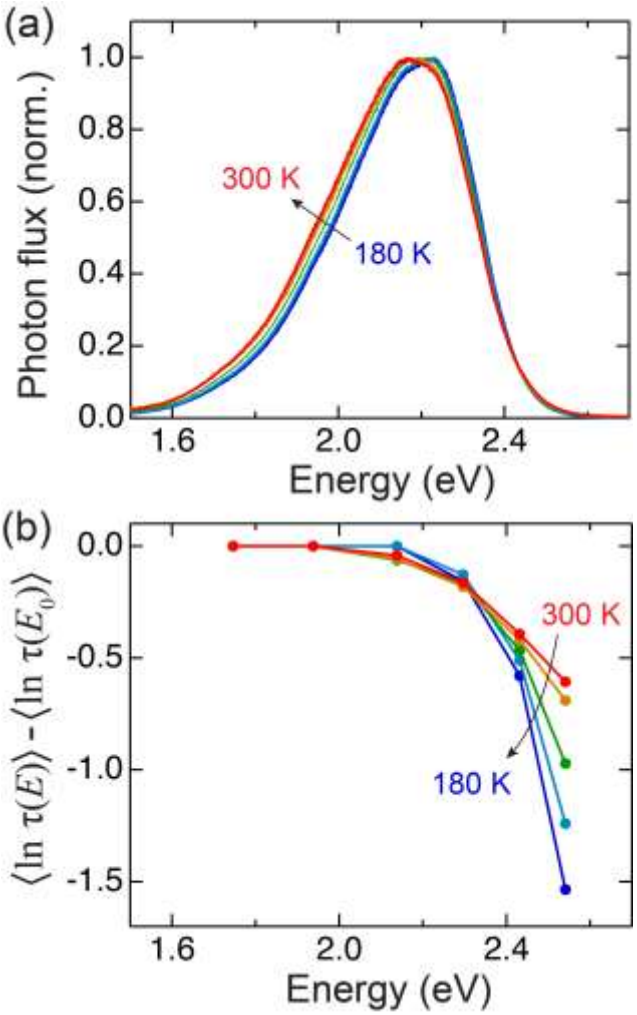

Figure 4. (a) DC EL spectra of the device from Figure 3a,b recorded at different temperatures. **(b)** Change in average logarithmic recombination time constant measured across the EL spectrum (relative to the low energy tail at $E_0 = 1.75$ eV) via MELS over the same range of temperatures at a constant DC current density of 2 mA cm^{-2}.

The observation of dispersive EL in Figure 3a,b unequivocally answers two important questions about CT states in MTDATA:BPhen OPV cells. First, it confirms that static disorder

(inhomogeneous broadening associated with different CT state site energies that collectively make up the CT DOS) contributes significantly to the CT EL lineshape, which has recently been the subject of debate [30,38–40]. If dynamic disorder (homogeneous broadening associated with CT state thermal fluctuations) were the sole contribution, the MELS frequency response would be independent of photon energy since the molecular vibrations that broaden the emission in this case happen on a much faster (ps) timescale than MELS probes (<MHz). In other words, the only way that CT emission at one photon energy can have a different MELS phase delay (i.e. time lag) relative to that at another energy is if they arise from energetically different CT states with different formation/decay dynamics (i.e. an inhomogeneously-broadened ensemble). Supplementary Figure S1 provides a visual illustration of this point.

Second, dispersive CT EL demonstrates that CT states occupying the disorder-induced DOS are not in in quasi-equilibrium with one another. If they were, the MELS response would again be independent of photon energy since fast equilibration (i.e. faster than all other timescales of charge transport and recombination) within the CT DOS would ensure that CT states at different energies all respond to the MELS perturbation at the same time with no energy-dependent phase delay. Another way of saying this is that if the CT state distribution were characterized by a quasi-equilibrium occupation function, the MELS perturbation would affect the entire occupation function (e.g. via a change in chemical potential), causing CT states at all energies to respond in unison and thus exhibit the same phase in the MELS spectrum.

2.3. Model for dispersive CT emission

At a basic level, dispersive CT state EL could arise from an energy-dependent CT state formation rate (τ_{rec}^{-1}), an energy-dependent CT state decay rate (τ_{ct}^{-1}), or both. The first possibility was postulated in Ref. [5] and is generally expected for OPVs on the basis of **Figure 5a** since the lowest energy CT states result from the recombination of electrons and holes within the tails of their respective DOS ($g_{\mathrm{n}}(E)$ and $g_{\mathrm{p}}(E)$, respectively). Because these carriers are the least mobile, and the recombination rate is proportional to their mobility (nominally via the Langevin rate coefficient), the formation rate of low energy CT states is expected to be slower than that of higher energy CT states formed from more mobile carriers that are higher in the free carrier DOS. Low energy CT states are therefore less capable of responding to the MELS current modulation at high frequency. In short, dispersive electron and hole mobilities imply energy-dependent electron and hole mobilities, and thus also an energy-dependent rate of CT state formation.

Energy-dependent CT state decay may also occur insofar as high energy CT states relax toward lower energy on a timescale that is comparable to their natural radiative and non-radiative decay. The existence of this mechanism is supported by a dynamic red-shift (i.e. spectral diffusion)[7] of the CT state PL observed for MTDATA:BPhen films in the Supplementary Material. Higher energy CT states consequently have a shorter lifetime than lower energy CT states (since the rate of relaxation competes with radiative and non-radiative decay for higher energy CT states, but not for lower energy CT states) and can therefore be modulated at higher frequency. In principle, there should also be a Cole-Davidson exponent associated with the τ_{ct} pole in $\widetilde{H}_{\mathrm{MELS}}$; however, since including both exponents would lead to a highly correlated fit, we neglect it out of practical necessity. Note that the CT state radiative decay rate is not expected to depend on energy whereas the intrinsic non-radiative decay rate (via electron-phonon coupling to the ground state) is, if anything, expected to increase at lower energy due to the energy gap law[25]. Since the latter is

opposite to the MELS data, we conclude that an energy-dependent intrinsic CT state lifetime does not contribute to the observed EL dispersion.

As a first attempt at modeling dispersive CT MELS, we focus solely on energy-dependent CT state formation because 1) it is sufficient to reproduce most of our observations, 2) relaxation is expected to be less important for CT EL than PL, and 3) incorporating relaxation greatly complicates the model. Assuming encounter-dominated Langevin electron-hole recombination[11], the formation rate of CT states with a given energy, E_{ct}, is:

$$K_{\mathrm{rec}}(E_{\mathrm{ct}}) = \int \frac{q}{\varepsilon}\left[\mu_{\mathrm{n}}(E_{\mathrm{n}}) + \mu_{\mathrm{p}}(E_{\mathrm{p}})\right] n(E_{\mathrm{n}}) p(E_{\mathrm{p}}) dE_{\mathrm{p}} \,, \tag{5}$$

where ε is the dielectric constant of the organic semiconductor and the electron energy (E_{n}) is related to the hole energy (E_{p}) via the CT state binding energy (E_{b}) according to $E_{\mathrm{n}} = E_{\mathrm{p}} + E_{\mathrm{ct}} + E_{\mathrm{b}}$, as illustrated in Figure 5a. For simplicity, we assume E_{b} is a constant, though in general there will be a distribution of binding energies as well[25]. We assume quasi-equilibrium electron and hole densities ($n(E_{\mathrm{n}})$ and $p(E_{\mathrm{p}})$) given by the product of their respective DOS and Fermi-Dirac occupation functions. Though the explicit energy dependence of the electron and hole mobilities ($\mu_{\mathrm{n}}(E_{\mathrm{n}})$ and $\mu_{\mathrm{p}}(E_{\mathrm{p}})$) in Equation (5) may appear unfamiliar within the context of OPV, it is central to the description of organic semiconductor thermoelectric properties[41,42].

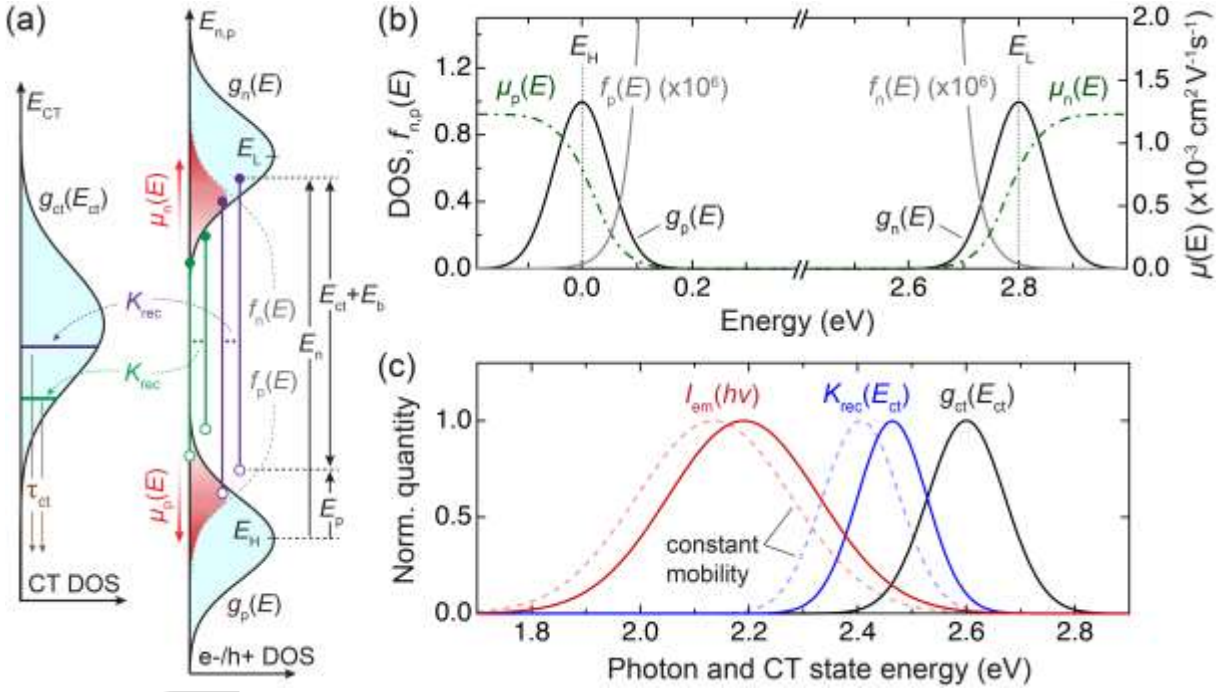

Figure 5. (a) Sketch of the relationship between the free carrier and CT state DOS. The red shaded regions indicate the electron and hole distributions given by the overlap of their respective DOS ($g_{\mathrm{n}}(E)$ and $g_{\mathrm{p}}(E)$) and Fermi-Dirac occupation functions ($f_{\mathrm{n}}(E)$ and $f_{\mathrm{p}}(E)$); the gradient in the shading conveys the energy-dependent mobility of each carrier. Because low energy CT states are formed from tail state electrons and holes with low mobility, and the Langevin recombination rate is proportional to mobility, low energy CT states respond more slowly to the MELS perturbation than high energy CT states. **(b)** Idealized system assuming a Gaussian electron and hole DOS with equal broadening (standard deviation, $\sigma_{\mathrm{n}} = \sigma_{\mathrm{p}} = 50$ meV) and a 2.8 eV gap between the mean highest occupied and lowest unoccupied molecular orbital energies (E_{H} and E_{L}, respectively). Gray lines show the room temperature electron and hole Fermi-Dirac occupation functions at a quasi-Fermi level splitting of 1.9 eV along with energy-dependent carrier mobilities calculated as in Ref. [41]. **(c)** Energy-dependent rate of CT state formation calculated for constant (blue dashed line) and energy-dependent (solid blue line) electron and hole mobilities. The red lines show the corresponding CT

emission spectra that result from convolving these distributions with the homogeneous CT state lineshape discussed in the text. In this model, the CT state distribution (which is directly proportional to the formation rate) accounts for approximately 12% of the full-width half-max emission linewidth, while the balance is due to homogeneous broadening from Equation 6. The details of each contribution, as well as a summary of all the model parameters, are provided in the Supplementary Material.

Assuming as in Equation (1) that, once formed, CT states decay to the ground state without relaxing or re-dissociating, then the steady-state CT distribution is directly proportional $K_{\mathrm{rec}}(E_{\mathrm{ct}})$; see Supplementary Material Section S8 for details. The CT emission spectrum is therefore obtained by convolving $K_{\mathrm{rec}}(E_{\mathrm{ct}})$ with the homogeneous CT lineshape given by Marcus electron transfer theory[23,39]:

$$g_{\mathrm{h}}(h\upsilon) = \frac{f_{\mathrm{em}}}{\sqrt{4\pi\lambda k_{\mathrm{b}}T}} \exp\left[\frac{-(E_{\mathrm{ct}} - \lambda - h\upsilon)^2}{4\lambda k_{\mathrm{b}}T}\right]. \quad (6)$$

In this expression, $h\upsilon$ is the photon energy, f_{em} is proportional to the square of the transition dipole moment, λ is the reorganization energy, k_{b} is Boltzmann's constant, and T is the temperature. The emitted photon flux per unit energy is therefore $I_{\mathrm{em}}(h\upsilon) \propto (h\upsilon)^3 K_{\mathrm{rec}}(E_{\mathrm{ct}}) * g_{\mathrm{h}}(h\upsilon)$, where the cubic factor of $h\upsilon$ accounts for the energy-dependence of the optical density of states[39,43–45].

Figure 5b shows an example of this calculation for an idealized system assuming a 2.8 eV gap between Gaussian electron and hole DOS functions with a constant CT state binding energy of $E_{\mathrm{b}} = 0.2$ eV. The resulting CT DOS is shown in Figure 5c along with the energy-dependent CT state formation rate that results from using Equation (5) with energy-dependent mobilities (Figure 5b) as

well as average, energy-independent mobilities for comparison. Whereas the latter is consistent with a CT state distribution given by room temperature ($T = 300$ K) Fermi-Dirac occupation of the CT DOS, the blue-shifted curve in the energy-dependent mobility case can only be approximated by Fermi-Dirac occupation using an effective temperature of ~420 K as detailed in the Supplementary Material. Thus, merely having energy-dependent electron and hole mobilities (or more specifically an energy-dependent Langevin rate coefficient) is sufficient to yield non-thermal CT state occupation, even when the electron and hole distributions themselves are in quasi-equilibrium at the ambient temperature.

Figure 6a,b shows that extending the MELS model from Equation (1) to include the energy-dependent Langevin rate in Equation (5) (see the Supplementary Material for details) leads to the type of dispersive behavior observed experimentally in Figure 3a,b. In contrast, an energy-independent Langevin rate coefficient based on average electron and hole mobilities yields a dispersionless response (red line). Hence, within this model, dispersive CT MELS is a hallmark of the type of non-thermal CT state distribution associated with the solid blue line in Figure 5c.

Given that the electron and hole mobilities of Alq_3 and NPB are likely just as energy-dependent as those of BPhen and MTDATA[46], it is reasonable to ask why the OLED MELS data are not dispersive. The answer has to do with differences in energy correlation between the highest occupied and lowest unoccupied molecular orbitals (HOMO and LUMO, respectively) that make up Frenkel excitons versus CT states. Whereas CT state energy is negatively correlated with variations in donor HOMO and acceptor LUMO energy (i.e. a high donor HOMO and low acceptor LUMO produces a small CT state energy), Frenkel exciton energy is positively correlated with the on-site HOMO and LUMO energies (i.e. for a given exciton energy, a molecule with a high HOMO has a high LUMO and vice versa)[47]. Thus, recombination of tail state electrons and holes does not preferentially produce

low energy Frenkel excitons as it does in the CT state case, leading to an energy-independent MELS response.

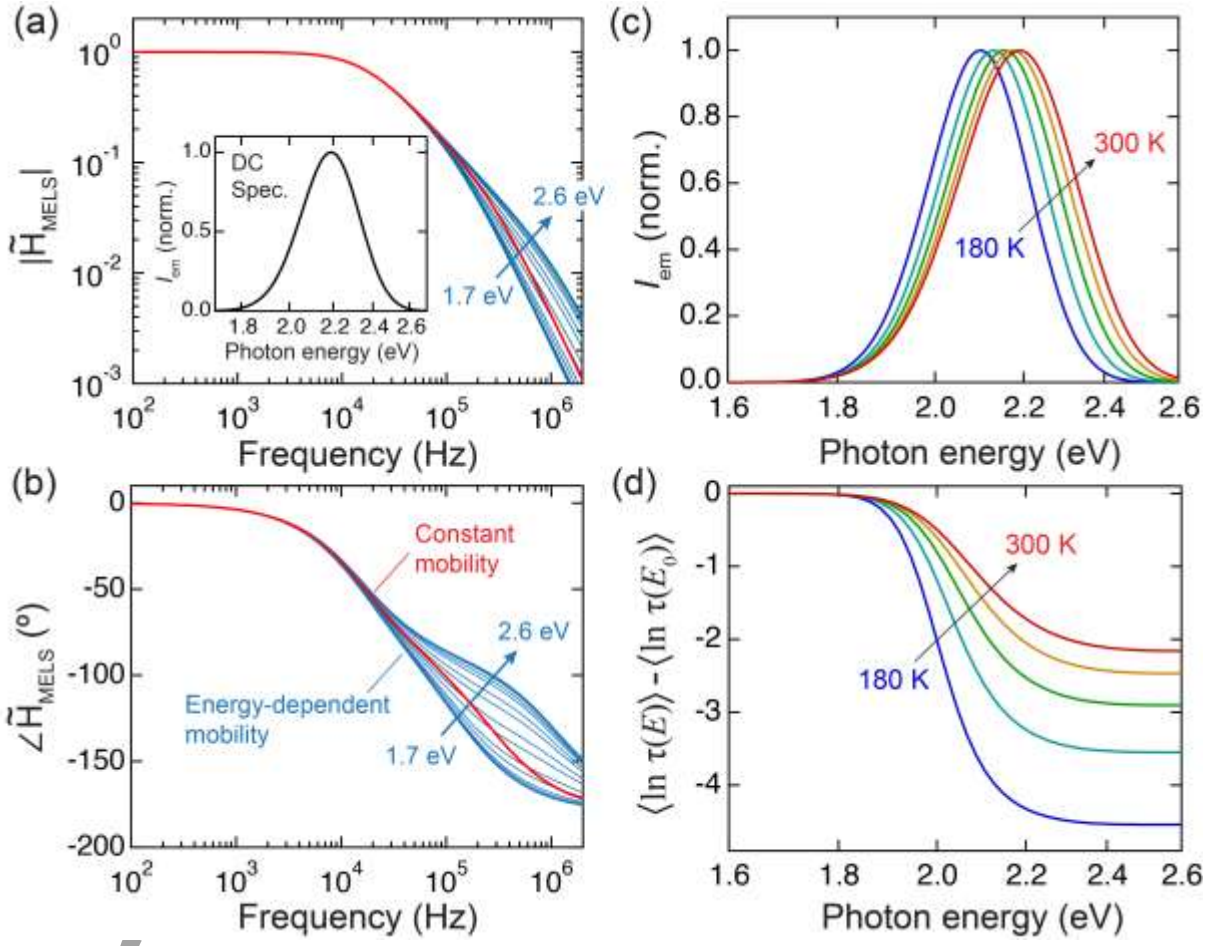

Figure 6. (a) Magnitude of the MELS response at different photon energies predicted for the idealized system in Figure 5b,c for the case of energy-dependent electron and hole mobilities (blue lines), and for the case of an average, energy-independent mobility (red lines, which are all stacked on top of one another). **(b)** Associated phase of the MELS response. **(c)** Temperature dependence of the simulated DC EL spectra for the energy-dependent mobility case. **(d)** Simulated variation in average logarithmic electron-hole recombination time (i.e. formation time for CT states) across the EL spectra in (c).

Figure 6d shows that the MELS model predicts increasing variation in $\langle \ln \tau \rangle$ across the CT emission spectrum as temperature decreases, in qualitative agreement with the data in Figure 4b, though the absolute change in $\langle \ln \tau \rangle$ is larger than observed. The fact that the DC EL spectrum predicted by the model (Figure 6c) red-shifts with decreasing temperature, whereas the data in Figure 4a do not, may be a consequence of neglecting CT state relaxation. Since CT states relax (either geminately[16] or via dissociation and reformation[11]) more efficiently at high temperature, accounting for relaxation would shift the high temperature spectra in Figure 6c closer to the 180 K spectrum, resulting in closer agreement with the data.

Progressing to a more comprehensive MELS model is a natural next step. This could be done via small-signal non-equilibrium drift-diffusion simulations[48,49] or, ideally, the same kMC methods that motivated non-equilibrium effects in OPVs to begin with[5,50]. By providing a direct and stringent constraint on CT state formation, relaxation, and recombination, spectrally-resolved MELS provides a useful tool to test and refine these models for application to more technologically-relevant OPV DA systems. We note that, in principle, time domain transient EL measurements provide the same information as MELS since the two are related via a Fourier transform. In practice, however, measuring in the frequency domain provides greater sensitivity to long time CT dynamics (e.g. associated with relaxation and non-geminate recombination) that are difficult to isolate from the baseline of, e.g. a pulsed streak camera transient.

3. Conclusion

In summary, we have carried out MELS on small molecule OPV cells and found that the frequency response of the high energy side of the CT EL spectrum is different than that of the low energy side. This observation confirms that static disorder-induced inhomogeneous broadening contributes substantially to the linewidth of the EL spectrum, and is unambiguous proof that the distribution of CT states formed by electrical injection in the dark is not in quasi-equilibrium. While other DA systems and other morphologies may behave differently, these results emphasize the need for caution when analyzing OPV cells on the basis of drift-diffusion and reciprocity models that assume quasi-equilibrium holds. To the extent that it does not, there may be new opportunities[51] to exploit this unusual behavior for improved device performance.

4. Materials and Methods

Sample preparation

Devices are fabricated by vacuum thermal evaporation in a chamber with a base pressure of 10^{-7} Torr on pre-patterned indium-tin-oxide (ITO) glass with a sheet resistance of 15 Ohms/sq. Sublimed-grade MTDATA and BPhen are purchased from Lumtec and used as received. The bulk heterojunction device structure is ITO/MTDATA (10 nm)/1:1 MTDATA:BPhen (60 nm)/BPhen (10 nm)/LiF (0.5 nm)/Al (100 nm), whereas that of the planar heterojunction devices is ITO/MTDATA (60 nm)/BPhen (60 nm)/LiF (0.5 nm)/Al (100 nm). The Alq_3/NPB device structure is ITO/NPB (100 nm)/Alq_3 (100 nm)/LiF (0.5 nm)/Al (100 nm). In all cases, the LiF/Al cathode is deposited through a shadow mask, which yields a 1x1 mm^2 device active area defined by the overlap with the patterned ITO. Following deposition, the devices are packaged within a N_2-filled glovebox using a bead of ultraviolet-curable epoxy and a glass lid.

Characterization

Impedance spectroscopy and MELS are carried out using a Zurich Instruments MFIA impedance analyzer. Electroluminescence is collected with a lens and focused onto a H10721 Hamamatsu photomultiplier tube (PMT; spectral responsivity range 230-870 nm) integrated with a 300 MHz bandwidth C11184 Hamamatsu transimpedance amplifier. Devices are driven between the force terminals of the impedance analyzer while the output signal from the transimpedance amplifier is detected between the sense terminals at 50 Ω load resistance. Energy resolution is obtained by placing a series of 10 nm bandwidth optical bandpass filters in front of the PMT along with a variable neutral density filter to maintain the total optical power input to the PMT within its optimal detection range. The AC modulation amplitude used for MELS is typically 200 mV and is superimposed on a DC bias selected to obtain a given DC current density; maintaining the DC current density <10 mA cm^{-2} yields stable and reproducible MELS data.

Steady-state EL and photoluminescence (PL) spectra are collected using a fiber-coupled spectrometer with a cooled Si CCD array. The PL is collected using an excitation wavelength of 350 nm with an approximate intensity of 8 mW/cm^2. In contrast to EL, the CT state PL of MTDATA:BPhen blends is unstable and visibly decreases in intensity over the span of a few minutes of continuous illumination at room temperature. Time-resolved PL spectra are acquired using a Hamamatsu C10910 streak camera synced to an optical parametric oscillator outputting ~20 ps pulses at 1 kHz repetition rate with an excitation wavelength of 375 nm and a pulse fluence of 0.4 $\mu J/cm^2$, respectively. Low temperature MELS measurements are carried out in a continuous flow Janis cryostat using coaxial electrical connections and a temperature diode adhered directly to the surface of the sample. Photovoltaic external quantum efficiency measurements employ an Energetiq laser-

driven Xe light source filtered through a monochromator and a lock-in amplifier for synchronous photocurrent detection.

Supporting Information

Supporting Information is available from the Wiley Online Library or from the author.

Acknowledgements

This work was supported by the U.S. Department of Energy, Office of Basic Energy Sciences under Award Nos. DE-SC0012365 and DE-SC0012458.

Received: ((will be filled in by the editorial staff))

Revised: ((will be filled in by the editorial staff))

Published online: ((will be filled in by the editorial staff))

References

[1] J. Nelson, *The Physics of Solar Cells*, Imperial College Press, London, **2004**.

[2] P. Würfel, U. Würfel, *Physics of Solar Cells*, Wiley-VCH Verlag GmbH, Weinheim, **2016**.

[3] A. Melianas, V. Pranculis, A. Devižis, V. Gulbinas, O. Inganäs, M. Kemerink, *Adv. Funct. Mater.* **2014**, *24*, 4507.

[4] A. Melianas, V. Pranculis, Y. Xia, N. Felekidis, O. Inganäs, V. Gulbinas, M. Kemerink, *Adv. Energy Mater.* **2017**, *7*, 1602143.

[5] A. Melianas, N. Felekidis, Y. Puttisong, S. C. J. Meskers, O. Inganäs, W. M. Chen, M. Kemerink, *Proc. Natl. Acad. Sci. U. S. A.* **2019**, *116*, 23416.

[6] A. Melianas, F. Etzold, T. J. Savenije, F. Laquai, O. Inganäs, M. Kemerink, *Nat. Commun. 2015 61* **2015**, *6*, 1.

[7] A. N. Brigeman, M. A. Fusella, B. P. Rand, N. C. Giebink, *Phys. Rev. Appl.* **2018**, *10*, 034034.

[8] S. Roland, J. Kniepert, J. A. Love, V. Negi, F. Liu, P. Bobbert, A. Melianas, M. Kemerink, A. Hofacker, D. Neher, *J. Phys. Chem. Lett.* **2019**, *10*, 1374.

[9] V. M. Le Corre, A. R. Chatri, N. Y. Doumon, L. Jan, A. Koster, V. M. Le Corre, A. R. Chatri, N. Y. Doumon, L. J. A. Koster, *Adv. Energy Mater.* **2017**, *7*, 1701138.

[10] N. J. Van Der Kaap, L. J. A. Koster, *Sci. Reports 2016 61* **2016**, *6*, 1.

[11] G. Zuo, S. Shoaee, M. Kemerink, D. Neher, *Phys. Rev. Appl.* **2021**, *16*, 034027.

[12] N. Felekidis, A. Melianas, L. E. Aguirre, M. Kemerink, *Adv. Energy Mater.* **2018**, *8*, 1800419.

[13] V. M. Le Corre, A. Rahimi Chatri, N. Y. Doumon, L. Jan Anton Koster, V. M. Le Corre, A. Rahimi Chatri, N. Y. Doumon, L. J. A Koster, *Adv. Energy Mater.* **2018**, *8*, 1803125.

[14] H. Bässler, *Phys. status solidi* **1993**, *175*, 15.

[15] P. M. Borsenberger, E. H. Magin, M. Der Van Auweraer, F. C. De Schryver, *Phys. Status Solidi* **1993**, *140*, 9.

[16] P. B. Deotare, W. Chang, E. Hontz, D. N. Congreve, L. Shi, P. D. Reusswig, B. Modtland, M. E. Bahlke, C. K. Lee, A. P. Willard, V. Bulovic, T. Van Voorhis, M. A. Baldo, *Nat. Mater. 2015 1411* **2015**, *14*, 1130.

[17] L. J. A. Koster, E. C. P. Smits, V. D. Mihailetchi, P. W. M. Blom, *Phys. Rev. B - Condens. Matter Mater. Phys.* **2005**, *72*, 085205.

[18] K. Vandewal, K. Tvingstedt, A. Gadisa, O. Inganäs, J. V. Manca, *Nat. Mater.* **2009**, *8*, 904.

[19] T. Kirchartz, B. E. Pieters, K. Taretto, U. Rau, *J. Appl. Phys.* **2008**, *104*, 094513.

[20] K. Vandewal, K. Tvingstedt, J. V. Manca, O. Inganäs, *IEEE J. Sel. Top. Quantum Electron.* **2010**, *16*, 1676.

[21] K. Vandewal, K. Tvingstedt, A. Gadisa, O. Inganäs, J. V. Manca, *Phys. Rev. B* **2010**, *81*, 125204.

[22] T. M. Clarke, J. R. Durrant, *Chem. Rev.* **2010**, *110*, 6736.

[23] K. Vandewal, *Ann. Rev. Phys. Chem.* **2016**, *67*, 113.

[24] S. U. Z. Khan, J. Bertrandie, M. Gui, A. Sharma, W. Alsufyani, J. F. Gorenflot, F. Laquai, D. Baran, B. P. Rand, *Joule* **2022**, *6*, 2821.

[25] Z. Zheng, N. R. Tummala, T. Wang, V. Coropceanu, J. L. Brédas, *Adv. Energy Mater.* **2019**, *9*, 1803926.

[26] Y. T. Fu, D. A. Da Silva Filho, G. Sini, A. M. Asiri, S. G. Aziz, C. Risko, J. L. Brédas, *Adv. Funct. Mater.* **2014**, *24*, 3790.

[27] T. Azuhata, T. Homma, Y. Ishikawa, S. F. Chichibu, T. Sota, T. Mukai, *Appl. Phys. Lett.* **2001**, *79*, 1100.

[28] K. Bansal, S. Datta, *J. Appl. Phys.* **2011**, *110*, 114509.

[29] R. S. Sánchez, A. Villanueva-Antolí, A. Bou, M. Ruiz-Murillo, I. Mora-Seró, J. Bisquert, R. S. Sánchez, A. Villanueva-Antolí, A. Bou, I. Mora-Seró, J. Bisquert, M. Ruiz-Murillo, *Adv. Mater.* **2023**, *35*, 2207993.

[30] S. U. Z. Khan, B. P. Rand, *Phys. Rev. Appl.* **2021**, *16*, 044026.

[31] L. Zhu, K. Xu, Y. Wang, J. Chen, D. Ma, *Front. Optoelectron.* **2015**, *8*, 439.

[32] S. Weissenseel, A. Gottscholl, R. Bönnighausen, V. Dyakonov, A. Sperlich, *Sci. Adv.* **2021**, *7*, 9961.

[33] S. Ullbrich, J. Benduhn, X. Jia, V. C. Nikolis, K. Tvingstedt, F. Piersimoni, S. Roland, Y. Liu, J. Wu, A. Fischer, D. Neher, S. Reineke, D. Spoltore, K. Vandewal, *Nat. Mater.* **2019**, *18*, 459.

[34] N. Bunzmann, S. Weissenseel, L. Kudriashova, J. Gruene, B. Krugmann, J. V. Grazulevicius, A. Sperlich, V. Dyakonov, *Mater. Horizons* **2020**, *7*, 1126.

[35] B. K. P. Scaife, *Principles of Dielectrics*, Clarendon Press, Oxford, **1998**.

[36] D. W. Davidson, R. H. Cole, *J. Chem. Phys.* **1951**, *19*, 1484.

[37] R. Zorn, *J. Chem. Phys.* **2002**, *116*, 3204.

[38] W. Gong, M. A. Faist, N. J. Ekins-Daukes, Z. Xu, D. D. C. Bradley, J. Nelson, T. Kirchartz, *Phys. Rev. B* **2012**, *86*, 024201.

[39] K. Tvingstedt, J. Benduhn, K. Vandewal, *Mater. Horizons* **2020**, *7*, 1888.

[40] F. J. Kahle, A. Rudnick, H. Bässler, A. Köhler, *Mater. Horizons* **2018**, *5*, 837.

[41] R. Schmechel, *J. Appl. Phys.* **2003**, *93*, 4653.

[42] D. Scheunemann, M. Kemerink, *Phys. Rev. B* **2020**, *101*, 075206.

[43] M. De Jong, L. Seijo, A. Meijerink, F. T. Rabouw, *Phys. Chem. Chem. Phys.* **2015**, *17*, 16959.

[44] B. Henderson, G. F. Imbusch, *Optical Spectroscopy of Inorganic Solids*, Clarendon Press,

Oxford, **1989**.

[45] A. Kohler, H. Bassler, *Electronic Processes in Organic Semiconductors*, Wiley-VCH, **2015**.

[46] A. Massé, P. Friederich, F. Symalla, F. Liu, R. Nitsche, R. Coehoorn, W. Wenzel, P. A. Bobbert, *Phys. Rev. B* **2016**, *93*, 195209.

[47] A. Massé, P. Friederich, F. Symalla, F. Liu, V. Meded, R. Coehoorn, W. Wenzel, P. A. Bobbert, *Phys. Rev. B* **2017**, *95*, 115204.

[48] N. Felekidis, A. Melianas, M. Kemerink, *Phys. Rev. B* **2016**, *94*, 035205.

[49] N. D. Nguyen, M. Schmeits, *Phys. status solidi* **2006**, *203*, 1901.

[50] M. Mesta, J. Cottaar, R. Coehoorn, P. A. Bobbert, *Appl. Phys. Lett.* **2014**, *104*, 213301.

[51] T. Upreti, C. Tormann, M. Kemerink, *J. Phys. Chem. Lett.* **2022**, *13*, 6514.

[52] C. L. Braun, *J. Chem. Phys.* **1984**, *80*, 4157.

[53] N. A. Drigo, L. G. Kudriashova, S. Weissenseel, A. Sperlich, A. J. Huckaba, M. K. Nazeeruddin, V. Dyakonov, *J. Phys. Chem. C* **2018**, *122*, 22796.

[54] S. N. Hood, I. Kassal, *J. Phys. Chem. Lett.* **2016**, *7*, 4495.

[55] T. M. Burke, S. Sweetnam, K. Vandewal, M. D. McGehee, *Adv. Energy Mater.* **2015**, *5*, 1500123.

Disorder in organic solar cells leads to an energetic distribution of charge transfer (CT) states. Modulation electroluminescence spectroscopy shows that higher energy CT states in this distribution respond to a voltage perturbation faster than lower energy CT states, confirming that they do not exist in quasi-equilibrium, even for devices operated in the dark.

Raju Lampande, Adrian Pizano, Manting Gui, Robert C. Cawthorn, Barry P. Rand, and Noel C. Giebink*

Dispersive charge transfer state electroluminescence in organic solar cells